

A new identity card for the bulge globular cluster NGC 6440 from resolved star counts*

CRISTINA PALLANCA,^{1,2} BARBARA LANZONI,^{1,2} FRANCESCO R. FERRARO,^{1,2} LUCA CASAGRANDE,³ SARA SARACINO,⁴
BHAVANA PUROHITH BHASKAR BHAT,^{1,2} SILVIA LEANZA,^{1,2} EMANUELE DALESSANDRO,² AND ENRICO VESPERINI⁵

¹*Dipartimento di Fisica e Astronomia, Università di Bologna, Via Gobetti 93/2, Bologna I-40129, Italy*

²*Istituto Nazionale di Astrofisica (INAF), Osservatorio di Astrofisica e Scienza dello Spazio di Bologna, Via Gobetti 93/3, Bologna I-40129, Italy*

³*Research School of Astronomy and Astrophysics, The Australian National University, Canberra, ACT 2611, Australia*

⁴*Astrophysics Research Institute, Liverpool John Moores University, 146 Brownlow Hill, Liverpool L3 5RF, UK*

⁵*Department of Astronomy, Indiana University, Bloomington, IN 47401, USA*

ABSTRACT

We present a new identity card for the cluster NGC 6440 in the Galactic Bulge. We have used a combination of high-resolution Hubble Space Telescope images, wide-field ground-based observations performed with the ESO-FORS2, and the public survey catalog Pan-STARRS, to determine the gravitational center, projected density profile and structural parameters of this globular from resolved star counts. The new determination of the cluster center differs by $\sim 2''$ (corresponding to 0.08 pc) from the previous estimate, which was based on the surface brightness peak. The star density profile, extending out to $700''$ from the center and suitably decontaminated from the Galactic field contribution, is best-fitted by a King model with significantly larger concentration ($c = 1.86 \pm 0.06$) and smaller core radius ($r_c = 6.4'' \pm 0.3''$) with respect to the literature values. By taking advantage of high-quality optical and near-infrared color-magnitude diagrams, we also estimated the cluster age, distance and reddening. The luminosity of the RGB-bump was also determined. This study indicates that the extinction coefficient in the bulge, in the direction of the cluster has a value ($R_V = 2.7$) that is significantly smaller than that traditionally used for the Galaxy ($R_V = 3.1$). The corresponding best-fit values of the age, distance and color excess of NGC 6440 are 13 Gyr, 8.3 kpc and $E(B - V) \sim 1.27$, respectively. These new determinations also allowed us to update the values of the central ($t_{rc} = 2.5 \cdot 10^7$ yr) and half-mass ($t_{rh} = 10^9$ yr) relaxation times, suggesting that NGC 6440 is in a dynamically evolved stage.

Keywords: Globular star Clusters: individual (NGC 6440); Globular star clusters: structural parameters; Milky Way Galaxy; Galactic bulge; HST photometry; Interstellar reddening; Interstellar extinction; Astrophysics - Solar and Stellar Astrophysics

1. INTRODUCTION

We are carrying out the project *Cosmic-lab*¹ aimed at using star clusters in the Local Universe as cosmic laboratories to study the complex interplay between the dynamical evolution of stellar systems and the properties of their stellar populations (e.g., Ferraro et al. 2012, 2018a,b, 2019; Lanzoni et al. 2016, 2018a,b, 2019). In fact, gravitational interactions among stars have a dramatic effect on the dynamical evolution of dense stellar systems like globular clusters (GCs), acting over time scales significantly shorter than their age and in a way that primarily depends on their internal properties (mass density, binary content, total mass, etc.) and the external environment (Galactic tide, disk shocks; e.g. Bailyn 1995; Meylan & Heggie 1997). Such interactions have been indicated also as an efficient channel for the formation of stellar exotica (like interacting binaries, blue stragglers and millisecond pulsars; Bailyn 1995; Pooley et al. 2003; Ransom et al. 2005; Ferraro et al. 2009a, 2016a; Pallanca et al. 2010, 2013, 2014, 2017; Dalessandro et al. 2014;

Corresponding author: Cristina Pallanca
cristina.pallanca3@unibo.it

* Based on observations collected with the NASA/ESA HST (Prop. 11685, 12517, 13410, and 15403), obtained at the Space Telescope Science Institute, which is operated by AURA, Inc., under NASA contract NAS5-26555. Also based on observations collected at the European Southern Observatory, Cerro Paranal (Chile), under proposal 077.D-0775(Bale).

¹ See the web page: <http://www.cosmic-lab.eu/Cosmic-Lab/Home.html>

Cadelano et al. 2017, 2018; Beccari et al. 2019). Indeed, the innermost core regions of GCs are expected to offer the ideal environment for the occurrence of stellar interactions able to generate exotic objects, including the long sought class of intermediate-mass black holes (e.g. Portegies Zwart et al. 2004; Giersz et al. 2015). For this reason, the accurate characterization of GCs in terms of structural properties, dynamical status and internal kinematics is a crucial step to properly understand how dynamical processes affect the evolutionary history of these systems and impact the formation of stellar exotica.

The systematic use of Hubble Space Telescope (HST) and, more recently, adaptive optics assisted observations has opened the possibility of constructing projected density profiles directly from star counts even for the innermost regions of high-density stellar systems, not only in the Galactic halo and bulge (e.g., Ferraro et al. 2009b; Saracino et al. 2015; Ferraro et al. 2021), but also beyond the Milky Way (Lanzoni et al. 2019). In spite of this, the vast majority of GC structural and morphological parameters currently available in largely used catalogs (e.g., Harris 1996; Mackey & Gilmore 2003; McLaughlin & van der Marel 2005) are still derived from surface brightness (SB) profiles. In previous papers (see Ferraro et al. 1999a, 2003; Lanzoni et al. 2007a,b,c, 2010, 2019; Mocchi et al. 2013), we demonstrated the advantage of determining the cluster structural parameters from individual star counts instead of SB. By construction, SB profiles directly depend on the luminosity of the surveyed stars and can therefore be artificially distorted by the sparse presence of luminous sources (see, e.g., Noyola & Gebhardt 2006, for the discussion of methods trying to correct for this problem) and/or reddening bubbles within the field of view (FOV). Instead, this has no impact on the density distribution obtained from resolved star counts since every object has the same weight independently of its luminosity. In addition, if proper motions can be measured, field stars (that may be particularly bright and substantially contribute to SB) can be explicitly excluded from the determination of the number count density profile. Hence, although SB can be helpful in cases of severe photometric incompleteness of the catalogs (e.g., Santos et al. 2020), it should be always used with caution, and number counts generally represent the most robust way for determining the cluster structural parameters (e.g. Lugger et al. 1995; Ferraro et al. 1999a, 2003). Moreover, once the cluster core is full resolved into individual stars, the determination of the center of gravity of the system becomes possible by simply averaging the coordinates of the detected stars. Indeed, we were among the first teams in promoting and adopting the center of gravity, instead of the center of luminosity, as optimal proxy of the cluster center (Montegriffo et al. 1995, see also Calzetti et al. 1993). However, apart from a few studies regarding individual or very small sets of clusters (e.g. Salinas et al. 2012), these techniques have not been fully exploited in the literature yet, because constructing complete samples of stars in the highly crowded central regions of GCs is not an easy task (Ferraro et al. 1997a,b; Raso et al. 2017).

Our group already published resolved star density profiles for stellar systems in different dynamical stages of their evolution (both pre- and post-core collapse GCs; see Lanzoni et al. 2010; Mocchi et al. 2013, and Ferraro et al. 2003, 2009a; Dalessandro et al. 2013, respectively), both in the Galaxy and in the Large Magellanic Cloud (Lanzoni et al. 2019). Here we present the determination of the star density profile and the structural parameters for the bulge GC NGC 6440, for which we recently built a high-resolution extinction map able to correct for the strong differential reddening effects in the direction of the cluster (Pallanca et al. 2019). The paper is organized as follows. In Section 2 we describe the used dataset and the main steps of the data analysis. The procedure adopted to determine the gravity center is reported in Section 3. In Section 4 we describe the method used to obtain the observed star count profile and the determination of the structural parameters through its fit with the King model family. Section 5 reports the estimate of the distance modulus and the age. The identification of the RGB-bump and the comparison with the literature is presented in Section 6. Finally, in Section 7 we discuss the main results and we summarise the conclusions.

2. OBSERVATIONS AND DATA ANALYSIS

To properly sample the entire radial extension of NGC 6440, in the present work we used a combination of high-resolution and wide-field images, complemented with catalogs from public surveys.

The highly crowded central regions of the system have been investigated by means of HST data, consisting in a series of deep images acquired with the Wide Field Camera 3 (WFC3) through different filters (especially, F606W and F814W) and in various epochs (see Table 1). This is essentially the same dataset used in Pallanca et al. (2019) to construct the extinction map in the direction of the cluster. Hence more details can be found there. Here we just remind that this dataset provides us with two different samples: (a) the *HST-PM sample* including all the stars with measured proper motion (PM), thus allowing the decontamination from possible non-cluster members (Galactic

field stars), and (b) the *HST-noPM sample* including also the stars observed in only one epoch (hence, with no PM measure) and covering a larger area on the plane of the sky.

For the intermediate cluster region, we used ground-based data acquired with the FOcal Reducer/low dispersion Spectrograph 2 (FORS2) mounted at the ESO Very Large Telescope at Paranal Observatory (Chile) and retrieved from the ESO Science Archive. The FORS2 imaging detector consists of a mosaic of two 2000x4000 pixel MIT CCDs (15 $\mu\text{m}/\text{pixel}$) that combines a relatively large FOV ($6.8' \times 6.8'$) and reasonably high-resolution capabilities (pixel size of $\sim 0.25''$) for the standard resolution set up. The core of the cluster is roughly located at the center of the FORS2 FOV. Only one image in the V_{BESS} and one in the I_{BESS} filters were available for NGC 6440.

To properly sample the cluster outskirts and beyond, we retrieved (from <https://catalogs.mast.stsci.edu/panstarrs/>) the Pan-STARRS catalog for a circular region of $700''$ radius centered on NGC 6440. The Panoramic Survey Telescope and Rapid Response System (Pan-STARRS) is a wide-field photometric survey operated by the Institute for Astronomy at the University of Hawaii, performed with a 1.4 Gigapixel camera (GPC1) mounted at a 1.8 meter telescope, in five broad-band filters (g, r, i, z, y). For the present analysis we used only i and r data.

The detailed description of the data analysis procedure for the HST dataset can be found in [Pallanca et al. \(2019\)](#). Here we just summarize the main steps. The photometric analysis has been carried out by using the DAOPHOT package ([Stetson 1987](#)). The point spread function (PSF) for each image has been modelled on several bright and isolated stars, by using the DAOPHOTII/PSF routine. Then PSF-fitting photometry has been performed independently on all the images by imposing a source detection threshold more than $5\text{-}\sigma$ above the background level and, a master list has been produced considering as reliable sources all the objects measured in more than half of the images in at least one filter. We then run the ALLFRAME package ([Stetson 1987, 1994](#)) that simultaneously determines the brightness of the stars in all the frames, while enforcing one set of centroids and one transformation between all the images. Finally, the magnitudes obtained for each star have been normalized to a reference frame and averaged. The photometric error was derived from the standard deviation of the repeated measures. The instrumental magnitudes have been calibrated to the VEGAMAG system by using the photometric zero points reported on the WFC3 web page². Geometric distortions have been corrected following the prescription of [Bellini et al. \(2011\)](#) and then reported to the absolute coordinate system (α, δ) as defined by the World Coordinate System by using a sample of stars in common with the publicly available Gaia DR2 catalog ([Gaia Collaboration et al. 2016a,b](#)). The resulting astrometric accuracy turns out to be $< 0.1''$.

A similar procedure was adopted in the analysis of the FORS2 wide-field dataset. In summary, per each exposure we modelled the PSF by using dozens of bright, isolated and non saturated stars and we applied such model to all the sources detected at $3\text{-}\sigma$ above the background level. In a second step we created a master list containing all the detected sources and for each object we forced the fit in both filters. The further step consisted in the creation of the catalog listing all the magnitudes measured in both filters. Finally, the instrumental positions have been reported to the absolute coordinate system by using a sample of stars in common with the Gaia DR2 catalog. In order to make the three catalogs homogeneous in magnitude, we calibrated the V_{BESS} and I_{BESS} magnitudes of FORS2 onto the HST F606W and F814W magnitudes, respectively, by using color equations obtained from a large number of stars in common between the two datasets. Then, we used the stars in common between Pan-STARRS and FORS2 to homogenize the r and i magnitudes of the former with the FORS2 magnitudes previously calibrated onto HST. Hence, at the end of the procedure, the magnitudes measured in the three datasets are all homogeneous and calibrated in the same (HST) system. From now on, we use the symbols V_{606} and I_{814} to indicate both the HST magnitudes, and the magnitudes of the other two datasets calibrated onto the F606W and the F814W bands, respectively.

Four catalogs have been obtained from the available datasets. The *HST-PM* catalog includes all the stars measured in the portion of the cluster where multi-epoch WFC3 images have been acquired. It has been corrected for differential reddening (see [Pallanca et al. 2019](#)) and decontaminated from Galactic field stars via PM analysis. It counts 137194 stars. The *HST-noPM* catalog is made of all the stars detected in the portion of the cluster surveyed by all the available WFC3 observations. It reports the observed magnitudes (with no correction for differential reddening) for a total of 174418 objects. The *FORS2* catalog contains 27487 stars measured in a roughly square region of $200''$ size around the cluster center. The *Pan-STARRS* catalog lists 40419 stars within a circle of $700''$ radius.

Figure 1 shows the spatial distribution of all the stars included in each of the four catalogs (blue dots), with respect to the cluster center. The corresponding color-magnitude diagrams (CMDs), which are plotted in Figures 2 and 3, are

² http://www.stsci.edu/hst/wfc3/phot_zp_lbn

Instrument Survey	Program ID	PI	Filter	$N_{\text{exp}} \times T_{\text{exp}}$
WFC3 [1]	GO 11685	Van Kerkwijk	F606W	1×392 s + 1×348 s
			F814W	1×348 s + 1×261 s
WFC3 [1]	GO 12517	Ferraro	F606W	27×392 s
			F814W	27×348 s
WFC3 [1]	GO 13410	Pallanca	F606W	5×382 s
			F814W	5×222 s
			F656N	10×934 s
WFC3 [1]			F606W	5×382 s
			F814W	5×222 s
			F656N	10×934 s
WFC3 [1]			F606W	5×382 s
			F814W	4×222 s + 1×221 s
			F656N	6×934 s + 2×864 s + 2×860 s
WFC3 [1]	GO/DD 15403	Pallanca	F606W	2×382 s
			F814W	1×223 s + 1×222 s
			F656N	2×969 s + 2×914 s
FORS2	077.D-0775(B)	Saviane	V_BESS	1×30 s
			L_BESS	1×30 s
GPC1 [2]			r	
			i	

Table 1. Summary of the used dataset. [1]=Pallanca et al. (2019), [2]=Pan-STARRS.

deep enough to trace the (cluster and field) stellar populations down to 3-4 magnitudes below the cluster Red Clump. Of course, an increasing population of field stars appears and becomes dominant with respect to cluster members for increasing distances from the cluster center, i.e., from the HST, to the FORS2, to the Pan-STARRS dataset.

3. DETERMINATION OF THE CENTER OF GRAVITY

As discussed in many previous papers (see, e.g., Montegriffo et al. 1995; Ferraro et al. 1997a, 1999a), dealing with resolved stars for the determination of the cluster center avoids introducing the bias induced by the possible presence of a few bright stars, which can generate a SB peak in an off-set position with respect to the true gravitational center. Here we thus took advantage of the *HST-PM* catalog, which properly samples the central region of the cluster, is corrected for the effects of differential reddening, and has been decontaminated from field star interlopers (see Figure 3). We used the same iterative procedure already adopted, e.g., in Lanzoni et al. (2007a,b, 2010, 2019), where the gravitational center (C_{grav}) is determined by averaging the (x, y) coordinates on the plane of the sky of all the stars observed in a selected range of magnitude and within a circle of radius r centered on a first-guess value (typically, the center quoted in the literature). We always adopt different values for the magnitude-cut and radius r , both to check the occurrence of possible dependencies of the result on these assumptions, and to estimate the uncertainty on the final position of C_{grav} . As discussed in Mocchi et al. (2013), the adopted values of r always exceed the core radius (r_c) quoted in the literature, to guarantee that the averaging procedure acts in a region where the density profile decreases with radius, i.e., is no more uniform (as it is, instead, in the innermost region). Taking into account that the literature values of r_c vary from $\sim 5''$ to $\sim 8''$ (see Table 2), we adopted $r = 15'', 20'', 30''$. As magnitude-cuts, we used reddening corrected $I_{814,0} < 18, 18.2, 18.5$, thus selecting approximately equal-mass samples, since the difference in mass between the stars at the main-sequence turnoff level and those in evolved evolutionary phases is quite small (within a few $0.01 M_{\odot}$). For every pair of magnitude-cut and r values, C_{grav} has been determined iteratively starting from the center quoted in the Harris (1996, 2010 edition) catalog and assuming that convergence is reached when ten consecutive iterations yield values of the cluster center that differ by less than $0.01''$ among them. As gravitational center of NGC 6440, we finally adopted the average of the values of C_{grav} obtained from this procedure, namely: $\alpha = 17^{\text{h}}48^{\text{m}}52.84^{\text{s}}$ and $\delta = -20^{\circ}21'37.5''$, with an uncertainty of $\sim 0.3''$. This is $\sim 2''$ east and $\sim 0.6''$ south from the

center quoted in the Harris (1996) catalog. Such a difference can have a non negligible impact on the derived shape of the star density profile and, more in general, on the study of the radial behavior of any stellar population within the cluster potential well.

4. STAR COUNT DENSITY PROFILE

In order to build the projected star density profile, $\Sigma_*(r)$, along the entire cluster radial extension, we combined the available photometric data-sets as follows: the *HST-noPM catalog* covers the innermost cluster regions ($\leq 115''$), the *FORS2 catalog*, where the center remains unresolved because of stellar crowding, is used to sample the intermediate regions ($115'' < r \leq 200''$), and the *Pan-STARRS catalog* refers to the outermost cluster regions ($200'' < r \leq 700''$). We considered only stars brighter than $I_{814} < 18.5$ (i.e., ~ 2 mag above the main-sequence turnoff; black dots in the top-right and bottom panels of Figure 1 and in Figure 2), because this limit ensures comparable levels of (high) photometric completeness, in combination with high enough statistics (thousands of stars) in all the catalogs. Following the standard procedure already adopted in several previous works (see Lanzoni et al. 2019 and references therein), we divided each photometric sample in several concentric annuli centered on C_{grav} (see Figure 1), and split each annulus into an adequate number of sub-sectors (typically four). The number of stars lying in each sub-sector was counted, and the star surface density was obtained by dividing these values by the corresponding sub-sector area. The stellar density in each annulus was then obtained as the average of the sub-sector densities, and the standard deviation was adopted as the uncertainty.

The observed stellar density profile is shown in Figure 4 (upper panel), where different symbols refer to different catalogs (empty circles for HST, triangles for FORS2 and squares for Pan-STARRS) and the radius associated with each annulus is the midpoint of the radial bin. As can be seen, the contribution of the Galactic field starts to be evident for distances from the cluster center larger than $r > 100''$ (i.e. in the FORS2 data-set) and becomes dominant for $r > 200''$ (Pan-STARRS catalog). As expected, the spatial distribution of field stars is approximately uniform on the considered radial scale, thus producing a well defined plateau in the outermost portion of the density profile. Hence, the level of Galactic field contamination has been estimated by averaging the data-points aligned in the plateau (see the dashed line in Figure 4) and the (decontaminated) cluster profile, obtained after subtraction of the Galaxy background level, is finally shown in Figure 4 (top panel; filled symbols). As apparent, after the field subtraction, the profile remains almost unchanged at small radii, which are in fact dominated by the cluster population, while it significantly decreases in the most external regions, where it turns out to be significantly below the Galactic background. This clearly indicates that an accurate measure of the field level is crucial for the reliable determination of the outermost portion of the density profile.

The background subtraction has a well-perceivable effect also in the region sampled by HST data. We thus took advantage of the *HST-PM catalog*, which is already cleaned from Galactic field interlopers, to double check the reliability of the adopted decontamination procedure. Thanks to the high level of completeness of the HST observations, we constructed the cluster density profile by using stars down to the sub-giant branch (i.e., 0.5 magnitudes deeper than the sample used in the previous procedure; black dots in the top-left panel of Figure 1), thus benefitting from a much larger statistics. Figure 4 (bottom panel) shows the density profile obtained from the *HST-PM catalog* (in red), vertically shifted to match the one obtained with the procedure described above (in blue): as can be seen, the two profiles are essentially identical in the common region, thus confirming the solidity of the adopted field decontamination approach.

In order to derive the physical parameters of the program cluster, we fit the observed star density profile with the family of King (1966) models in the isotropic, spherical and single-mass approximation. They constitute a *single-parameter* family, since their shape is uniquely determined by the dimensionless parameter W_0 , which is proportional to the gravitational potential at the center of the system, or, alternatively, to the ‘‘concentration parameter’’ c , defined as $c \equiv \log(r_t/r_0)$, where r_t and r_0 are the tidal and the King radii of the cluster, respectively.

The best-fit King model has been determined by exploring a grid of W_0 values varying between 0.4 and 12 in steps of 0.05, and selecting the solution that minimizes the χ^2 residuals between the observed and the theoretical density profiles (see Miocchi et al. 2013 and Lanzoni et al. 2019 for a detailed description of the adopted procedure and the method used to estimate the uncertainties). The resulting values of W_0 , concentration parameter, core, half-mass and tidal radii are: $W_0 = 8.10$, $c = 1.86$, $r_c = 6.4''$, $r_h = 50.2''$, $r_t = 481.4''$, respectively, with the uncertainties quoted in Table 2. The effective radius, defined as the radial distance including half the total number counts in projection (and corresponding to the projected half-light radius if SB, instead of resolved star density, is considered)

is $r_e = 36.8''$. The comparison with previous determinations in the literature shows significant discrepancies for all the parameters. In particular, the Harris catalog reports the values estimated by [McLaughlin & van der Marel \(2005\)](#), who found $c = 1.62$, $r_c = 8.1''$, $r_h = 44.8''$, $r_{\text{eff}} = 28.8''$, and $r_t = 354.9''$ (the values originally quoted in pc have been converted into arcseconds by using the cluster distance provided in that paper: $d = 8.4$ kpc). Hence, we find that NGC 6440 is more centrally concentrated than previously thought, with a smaller core radius and larger truncation radius, translating in a larger concentration parameter. The comparison with the values quoted by [Baumgardt & Hilker \(2018\)](#) is less straightforward because N-body simulations, instead of King models, are used there to fit the observation, and no uncertainties are provided. However, the provided values of core, half-mass and effective radii are consistent with ours within 10-20%. We also stress that SB (instead of number count) profiles and an offset position of the cluster centre are used in those studies, thus likely accounting for the different results. The density profile of some GCs is found to be best reproduced by [Wilson \(1975\)](#), instead of [King \(1966\)](#), models (see, e.g., [McLaughlin & van der Marel 2005](#); [Miocchi et al. 2013](#)). We thus compared the observations also with the [Wilson \(1975\)](#) model family, finding the best solution for $c = 3.30$, $r_c = 6.6''$ and $r_t \sim 230'$ (see the dotted line in the bottom panel Figure 4). Although the core radius is very similar to that obtained from the King fit, the Wilson model (that, by construction, provides a smoother cutoff at the limiting radius) severely overestimate the observed stellar density in the external portion of the profile. This is in agreement with the fact that NGC 6440 is orbiting the Bulge of our galaxy, where tidal truncation is expected to be more relevant than for faraway halo GCs.

5. THE DISTANCE MODULUS AND THE AGE OF NGC 6440

The distance modulus and the age of resolved stellar populations (as Galactic GCs) can be estimated through the comparison between the observed CMD and theoretical stellar isochrones, the main obstacle being the well known degeneracy of these parameters with the metallicity and the reddening.

In the case of NGC 6440, the metallicity is relatively well known since the first low-resolution spectroscopic measures (see [Armandroff & Zinn 1988](#); [Origlia et al. 1997](#); [Frogel et al. 2001](#)), indicating an overall iron abundance of the order of 1/3 - half solar. More recent high-resolution spectroscopy of small samples of giants measured in the IR ([Origlia et al. 2008a](#)) and in the optical band ([Muñoz et al. 2017](#)) confirmed a considerable iron content ($[\text{Fe}/\text{H}] = -0.5, -0.6$) with some α -enhancement ($[\alpha/\text{Fe}] = +0.3$), corresponding to a global metallicity³ $[\text{M}/\text{H}] \sim -0.4$.

The accurate estimate of the reddening, instead, is complicated by the fact that NGC 6440 is located close to the Galactic plane and toward the bulge, where the extinction law likely deviates from the canonical and commonly assumed behavior. An extensive discussion about extinction and reddening is presented in [McCall \(2004\)](#). Particular attention, however, has to be given to the extinction toward the inner Galaxy, where the R_V value is not constant and can significantly vary along different directions (e.g., [Popowski 2000](#); [Udalski 2003](#); [Nataf et al. 2013a](#); [Alonso-García et al. 2017](#), and references therein). Indeed, as discussed in [Nataf et al. \(2013a\)](#); [Casagrande & Vandenberg \(2014\)](#), and recently confirmed by [Ferraro et al. \(2021\)](#) and [C. Pallanca et al. \(2021, in preparation\)](#), the region toward the Galactic center seems to be better described by an extinction law with a significantly smaller value of R_V (even down to $R_V = 2.5$). Conversely some other authors found larger R_V values ($R_V = 3.2$) to be more appropriate (e.g., [Bica et al. 2016](#); [Kerber et al. 2019](#)). Hence, as already discussed by [Udalski \(2003\)](#), the proper dereddening of a particular field in the Galactic bulge might be difficult without prior determination of R_V along its line of sight.

The best way to constrain R_V in a specific direction is by simultaneously investigating the IR and the optical CMDs, which are, respectively, weakly and strongly sensitive to the true extinction law. To this purpose we used a combination of optical and IR catalogs of NGC 6440.

The adopted HST optical catalog was presented in [Pallanca et al. \(2019\)](#), while the IR one is based on deep J and K_s observations obtained with GeMS/GSAOI ([S. Saracino et al., 2021, in preparation](#)). For a proper comparison with stellar isochrones, we first corrected the CMDs obtained from these catalogs for the effect of differential reddening, which broadens and distorts the evolutionary sequences. To this end, we applied the procedure fully described in [Pallanca et al. \(2019\)](#) to the HST dataset. Briefly, we determined the reference mean ridge line of NGC 6440 using a sample of well-measured stars. Then, for every star in the HST catalog we selected a sample of close sources, thus defining a “local-CDM”. Finally, we estimated the value $\delta E(\text{B-V})$ necessary to superpose the reference mean ridge line onto the local-CMD and assigned this value to the corresponding investigated star. By construction, the $\delta E(\text{B-V})$ values thus obtained express the differential component of the reddening within the sampled FOV and can be positive

³ The global metallicity has been calculated through the relation reported by [Ferraro et al. \(1999b\)](#) and assuming $[\text{Fe}/\text{H}] = -0.56$ ([Origlia et al. 2008a](#))

or negative. This quantity, multiplied by the coefficient appropriate for the considered filter, is added to the observed magnitudes to get differential reddening corrected (DRC) magnitudes: $I_{814,DRC}$, $V_{606,DRC}$ (see Figure 5). Finally, for all the stars in common with the GeMS/GSAOI sample, the estimated values of $\delta E(B-V)$ have been used to correct also the IR magnitudes and build the corresponding differential reddening corrected CMD: K_{DRC} , $(J-K)_{DRC}$ (Figure 5).

To estimate the distance modulus and the age of NGC 6440, while constraining R_V , we then compared the differential reddening corrected CMDs with a set of PARSEC (Bressan et al. 2012) and Dartmouth (Dotter et al. 2008) isochrones of different ages computed for $[M/H] = -0.4$ in the four photometric bands of interest, namely, the WFC3 V_{606} and I_{814} filters, and the 2MASS J and K_s filters. To place the isochrones in the differential reddening corrected CMDs, we determined the values of the (temperature- and gravity-dependent) extinction coefficients in the four bands (namely, $R_{V_{606,i}}$, $R_{I_{814,i}}$, $R_{J,i}$ and $R_{K_s,i}$) for each i^{th} combination of effective temperature and surface gravity along every isochrone (Casagrande & Vandenberg 2014). This has been done by interpolating the values calculated for the MARCS grid (Gustafsson et al. 2008) under the assumption of the cluster metallicity and the Cardelli et al. (1989) extinction law with $R_V = 2.5$ and $R_V = 3.1$. A linear interpolation between these two limits then allowed us to determine the temperature- and gravity-dependent coefficients for intermediate values of R_V (between 2.5 and 3.1, stepped by 0.1).

We found that, under the assumption of $R_V = 3.1$, no combination of parameters is able to reproduce the optical and the IR CMDs simultaneously. In particular, a combination that well fits the optical CMD corresponds to an excessively bright and red isochrone in the IR, for both the considered models (see the black dashed lines in Figure 5). The problem becomes progressively milder for decreasing values of R_V , and the best solution is found for $R_V = 2.7$. Interestingly, similarly small values are needed to properly reproduce the observations of other GCs in the Galactic bulge (Ferraro et al. 2021, see also Pallanca et al. 2021, in preparation). The red lines shown in Figure 5 correspond to PARSEC and Dartmouth isochrones (upper and lower panels, respectively) computed under the assumption of $R_V = 2.7$, for an age of 13 Gyr, a distance modulus $\mu_0 = 14.60$ and an absolute color excess that is just slightly different between the two models: $E(B - V) = 1.28$ and 1.26, respectively. In particular, this combination of parameters not only well reproduces the horizontal branch magnitude level (see the PARSEC isochrones in the figure), but also best-fits the SGB/MS-TO region, which is the most sensitive to age variations. The best-fit solution has been evaluated through a χ^2 analysis, by determining, for each SGB/MS-TO star, the difference between its observed color and the color at the same magnitude level along the isochrones of 11, 12, 13 and 14 Gyr. As already done in previous papers (Ferraro et al. 2021; see also Saracino et al. 2016) the χ^2 parameter has been computed as the ratio between the square of this difference and the color along the isochrone, summed over all the selected stars. The best-fit model to the optical CMD and the χ^2 values as a function of the investigated ages are plotted, respectively, in the top and bottom panels of Figure 6. Taking into account the various uncertainties and degeneracies entering the fitting procedures, conservative estimates of the errors on the distance modulus and age are 0.1 mag and 1.5 Gyr, respectively.

Several previous works in the literature have been devoted to the determination of these parameters for NGC 6440. The study by Ortolani et al. (1994) is based on optical photometry, while the others have been performed in the IR, and in all cases the standard reddening law has been assumed. The only exception is the investigation of Kuchinski & Frogel (1995), who combined IR data with V band photometry and suggested that the anomalous colors observed for this cluster might require a non-standard reddening law. This is in agreement with our finding, although a detailed comparison between the proposed reddening laws is not obvious. Given the different R_V adoption, the comparison among various reddening determinations in the literature has to be done in terms of the extinction coefficient A_V , instead of the color excess $E(B-V)$, which is linked to the former by the following relation: $A_V = R_V \times E(B-V)$. Minniti (1995) quote $E(J-K) = 0.57$ and comment that this value is in good agreement with that of Ortolani et al. (1994), who found $E(B-V) = 1$ and adopt $R_V = 3$, corresponding to $A_V = 3$. Valenti et al. (2004a) quote $E(B-V) = 1.15$ and adopt $R_V = 3.1$, thus providing $A_V = 3.56$. From the Harris compilation, $A_V = 3.32$ is obtained for the standard value of R_V . The value estimated in the present study ($A_V = 2.7 \times 1.27 = 3.43$) therefore is within the range spanned by the results of previous works, which however do not correct for differential reddening, nor take into account the optical and IR CMDs simultaneously. Also the distance modulus here determined is in reasonable agreement with previous determinations and included between them: $\mu_0 = 14.64$ and 14.58 in Ortolani et al. (1994) and Valenti et al. (2004a), respectively. Finally, an age of 11_{-2}^{+3} Gyr was estimated by Origlia et al. (2008b) from pioneering adaptive optics photometry, and 13 Gyr is the value adopted by Muñoz et al. (2017) to fit the observed CMD with theoretical isochrones. These are both consistent with our determination of 13 ± 1.5 Gyr.

6. THE RGB-BUMP

The high-quality of the CMDs presented in this paper allows us to easily identify a well known evolutionary feature along the RGB: the so-called RGB bump. This feature appears in the CMD as a well defined clump of stars along the RGB. This evolutionary feature flags the moment when the H-burning shell reaches the H discontinuity left by the inner penetration of the convective envelope (see the seminal works by Fusi Pecci et al. 1990, Ferraro et al. 1991, 1992a,b and Ferraro et al. 1999b, 2000; see also the compilation by Zoccali et al. 1999, Riello et al. 2003 and Valenti et al. 2004b, and more recently by Nataf et al. 2013b). Figure 7 shows the differential luminosity function of the bright RGB stars in the differentially-corrected V_{606} , J , K bands. The well-defined peaks at $V_{606,DRC} = 18.84 \pm 0.05$, $J_{DRC} = 15.16 \pm 0.05$, $K_{DRC} = 14.04 \pm 0.05$ correspond to the RGB bump. Adopting the extinction and the distance reported in Table 2, we transformed the above values into absolute magnitudes obtaining $M_{V_{606}}^{Bump} = 1.12 \pm 0.12$, $M_J^{Bump} = -0.37 \pm 0.12$ and $M_K^{Bump} = -0.94 \pm 0.12$. In Figure 8 we show the comparison among these measures and previous determinations in the literature. In particular in the bottom and central panels of Figure 8 we show the nice agreement of the RGB bump magnitude in the IR bands with the estimates and the relations quoted in Valenti et al. (2004b). The situation appears to be much more complex in the optical V_{606} band, since the magnitude level found in the present study appears significantly brighter than that obtained by Nataf et al. (2013b), who quote $M_{V_{606}}^{Bump} = 1.48$. While the adopted extinction law and distance modulus are just slightly different between the two studies, most of the discrepancy is due to the observed RGB bump magnitude: $V_{606} = 19.431 \pm 0.021$ in Nataf et al. (2013b), $V_{606} = 18.9$ in our study. In addition, a metallicity as high as $[M/H]=+0.03$ has been assumed in that work.

Nevertheless, we note that the new determination of the RGB bump combined with the adopted metallicity well follows the trend of the GC distribution reported by Nataf et al. (2013b).

7. SUMMARY AND CONCLUSIONS

This work provides updated values for the structural parameters and age of NGC 6440, a GC in the direction of the Galactic bulge that is relatively poorly investigated because of the strong and differential extinction along its line of sight. To our knowledge, these are the first determinations of the center and density profile of NGC 6440 based on resolved star counts, which are free from biases induced by the possible presence of few bright objects. The gravitational center of the cluster has been determined from the observed positions of PM-selected member stars, and it turns out to be significantly off (by $\sim 2''$ in right ascension) with respect to the value quoted in the literature (Harris 1996), reporting the SB peak estimated by Picard & Johnston (1995). By making use of a suitable combination of high-resolution (HST) photometry and wide-field data (FOR2 observations and a Pan-STARRS catalogue), we then built the most radially extended surface density profile so far from resolved star counts. With respect to the work of McLaughlin & van der Marel (2005, see also the Harris catalog), which is based on the previous estimate of the cluster center and uses the SB distribution instead of number counts, the best-fit King model to the projected density profile derived in this work reveals that NGC 6440 has a significantly larger concentration parameter, a smaller core radius, and a larger overall extension (truncation radius) on the plane of the sky. The updated values of the cluster center and structural parameters are listed in Table 2.

By taking advantage of the PM selection, we built a sample of cluster member stars with both optical (HST) and IR (GeMS/GSAOI) magnitudes, that we properly corrected for the effect of differential reddening. We then used stellar isochrones, from both the PARSEC (Bressan et al. 2012) and the Dartmouth (Dotter et al. 2008) models, to simultaneously reproduce the optical and the IR CMDs (which are strongly and weakly dependent on reddening, respectively). Adopting extinction coefficients that depend on the stellar surface temperature and gravity, we explored extinction laws with R_V ranging from 2.5 to 3.1, and we found that $R_V = 2.7$ is required to fit both to the optical and the IR CMDs. This confirms (see also Popowski 2000; Nataf et al. 2013a; Casagrande & Vandenberg 2014) that the extinction law in Galactic regions close to the plane and in the direction of the bulge requires an R_V value significantly different from the “canonical” 3.1. The best-fit to the CMDs (in particular to the horizontal branch level, and the SGB/MS-TO region that strongly depends on the age of the stellar population) provided us also with the cluster age ($t = 13 \pm 1.5$ Gyr), distance modulus ($\mu_0 = 14.60 \pm 0.1$, corresponding to a distance of 8.3 kpc, with a conservative uncertainty of ~ 0.4 kpc), and absolute color excess, $E(B-V) = 1.26 - 1.28$, which corresponds to a V -band extinction coefficient $A_V = 3.34$. These values are all within the ranges spanned by previous determinations in the literature (see Section 5). In particular, the age estimate here obtained for NGC 6440 is the most accurate so far (although the uncertainty is still quite large: 1.5 Gyr). Figure 9 shows the age-metallicity distribution for the bulge GCs with available age estimate, where NGC 6440 is marked as a large red square. The data for the other clusters are mainly

from Saracino et al. (2019, see their Figure 16) and Oliveira et al. (2020, see their Figure 12) with the addition of the recent age determination of NGC 6256 (Cadelano et al. 2020). We also mark the age-metallicity of the oldest stellar population in the two Bulge Fossil Fragments (BFF; namely Terzan5 and Liller1) so far discovered into the bulge (Ferraro et al. 2009b, 2016b, 2021). The BFFs (Ferraro et al. 2009b, 2016b; Origlia et al. 2011; Massari et al. 2014) are systems that, in spite of their appearance as genuine GCs, host multi-age stellar populations and could be the remnants of massive clumps that contributed to form the bulge at the epoch of the Galaxy assembly. As apparent, these systems all have old ages, well consistent with those of the majority of bulge GCs and Galactic field stars observed in different directions toward the bulge (e.g., Zoccali et al. 2003; Clarkson et al. 2011; Valenti et al. 2013). The weighted mean age of the entire sample (now including a total of 18 GCs and 2 BFFs) is 12.7 ± 0.2 Gyr, which is ~ 0.5 Gyr older than the value quoted in Saracino et al. (2019) on the basis of a sub-sample of 14 objects.

The superb quality of the obtained CMDs allows an accurate determination of the RGB-bump. This value, combined with the spectroscopic estimate of the cluster metallicity, makes NGC 6440 to perfectly fit into the bump-metallicity relation defined by Galactic GCs.

The new determinations of the cluster structural parameters, distance and reddening allow us to also update the value of relaxation time of NGC 6440, which characterizes the dynamical evolutionary stage of the system. It quantifies the timescale needed by two-body interactions (causing kinetic-energy exchanges among stars) to bring the cluster toward a thermodynamically relaxed state. This quantity has been used to validate the so-called A^+ parameter, quantifying the level of central segregation of blue straggler stars within a GC (Alessandrini et al. 2016), as a powerful empirical diagnostic of the dynamical age of the host system (e.g., Ferraro et al. 2018a, 2019; Lanzoni et al. 2016; Ferraro et al. 2020). Primarily depending on the local density, the value of the relaxation time changes with the radial distance from the cluster center. To estimate the central relaxation time (t_{rc}) we used equation (10) of Djorgovski (1993). For the half-mass relaxation time (t_{rh}) we followed equation (8-72) of Binney & Tremaine (1987). The latter parameter can be estimated also from eq. (11) of Djorgovski (1993) once the first coefficient (8.993×10^5 in the equation) is substituted by its proper value (2.055×10^6 ; see Binney & Tremaine 1987; McLaughlin & van der Marel 2005). We also emphasize that the projected half-light radius r_e (instead of the three-dimensional half-mass radius r_h) is often used in this estimate (see, e.g., Harris 1996; McLaughlin & van der Marel 2005), under the implicit assumption that these radial scales are equal. However, depending on the value of the concentration parameter, the ratio between the effective and the half-mass radii varies between 0.73 and 0.76. As a consequence, since t_{rh} scales with half-mass radius at the power of 3/2, the relaxation time obtained by adopting r_e (t_{re}) is $\sim 35\%$ shorter than that calculated by using r_h . Assuming the absolute V -band magnitude and central SB quoted for NGC 6440 in the Harris (1996) catalog, and the same values adopted there for the average stellar mass ($0.3M_\odot$) and V -band mass-to-light ratio ($M/L_V = 2$), the new determinations of the structural parameters, distance, and extinction quoted in Table 2 bring to $\log(t_{rc}) = 7.4$ and $\log(t_{rh}) = 9.0$ (in units of year). If the effective radius is used in place of r_h (as it is done, e.g., in the Harris catalog and in McLaughlin & van der Marel 2005), the relaxation time becomes smaller than 1 Gyr: we find $\log(t_{re}) = 8.8$, which is 37% shorter than t_{rh} . For comparison, the central relaxation time quoted in the Harris (1996) catalog is $\log(t_{rc}) = 7.6$, i.e., a factor of ~ 1.6 longer than our determination, and the median relaxation time (8.62 in logarithmic units) is a factor of ~ 1.5 shorter than our value of t_{re} , mainly reflecting the scale-length differences discussed above, while the assumption of different extinction law and color excess has a negligible impact on the result. These values suggest that NGC 6440 is in a dynamically evolved stage (its age being much longer than the relaxation times), although the A^+ parameter has not been determined yet for this system, because a safe selection of its blue straggler population has been hampered so far by the large contamination from Galactic field stars and the severe and differential reddening conditions along its line of sight.

We thank the anonymous referee for useful comments that improved the presentation of the paper. This work is part of the project *Cosmic-Lab* at the Physics and Astronomy Department of the Bologna University (<http://www.cosmic-lab.eu/Cosmic-Lab/Home.html>). The research was funded by the MIUR throughout the PRIN-2017 grant awarded to the project *Light-on-Dark* (PI:Ferraro) through contract PRIN-2017K7REXT. The research is based on observations collected with the NASA/ESA HST (Prop. 11685, 12517, 13410 and 15403), obtained at the Space Telescope Science Institute, which is operated by AURA, Inc., under NASA contract NAS5-26555. LC is the recipient of the ARC Future Fellowship FT160100402. SS gratefully acknowledges financial support from the European Research Council (ERC-CoG-646928, Multi-Pop).

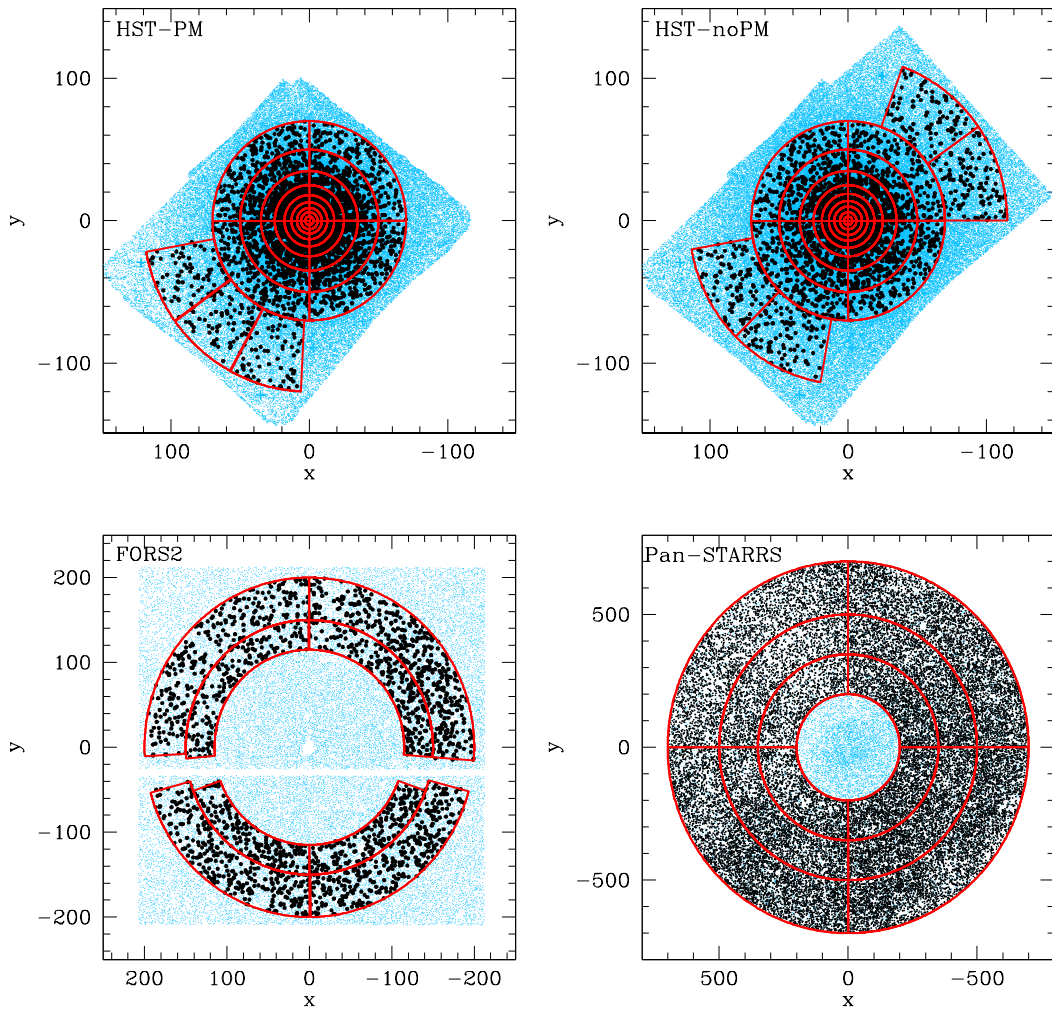


Figure 1. Spatial distribution of all the observed stars in each catalog (blue dots), with respect to the newly determined cluster center (see Table 2). The black dots correspond to the objects used to determined the cluster density profile: stars with $I_{814} < 19$ belonging to the HST-PM catalog (used to build the density profile shown in red in Figure 4) and stars with $I_{814} < 18.5$ in the other three datasets (used for the density profile shown in black in Figure 4). The red lines delineate the annuli and sub-sectors used to construct the density profile.

facilities:HST(WFC3/UVIS);ESO(FORS2)

REFERENCES

- Alessandrini, E., Lanzoni, B., Ferraro, F. R., et al. 2016, *ApJ*, 833, 252.
- Alonso-García, J., Minniti, D., Catelan, M., et al. 2017, *ApJL*, 849, L13.
- Armandroff, T. E. & Zinn, R. 1988, *AJ*, 96, 92
- Bailyn, C. D. 1995, *ARA&A*, 33, 133
- Baumgardt, H., & Hilker, M. 2018, *MNRAS*, 478, 1520
- Beccari, G., Ferraro, F. R., Dalessandro, E., et al. 2019, *ApJ*, 876, 87
- Bellini, A., Anderson, J., & Bedin, L. R. 2011, *PASP*, 123, 622
- Bica, E., Ortolani, S., & Barbuy, B. 2016, *PASA*, 33, e028. doi:10.1017/pasa.2015.47

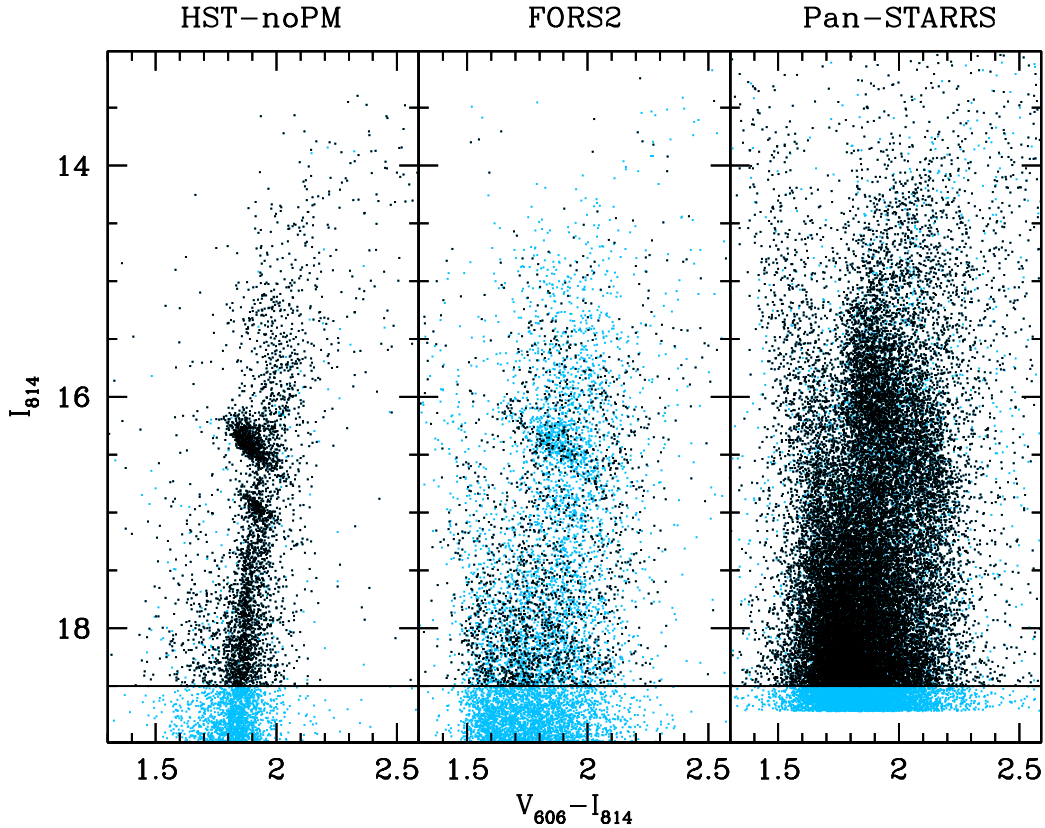


Figure 2. CMDs of NGC 6440 obtained from the *HST-noPM*, *FORS2* and *Pan-STARRS* catalogs discussed in the text (left, central, and right panel, respectively). The entire samples of surveyed stars are plotted in light blue, while the black dots highlight the stars used for the construction of the density profile.

- Bonatto, C., Campos, F., & Kepler, S. O. 2013, *MNRAS*, 435, 263
- Binney, J. & Tremaine, S. 1987, Princeton, N.J.: Princeton University Press, c1987.
- Bressan, A., Marigo, P., Girardi, L., et al. 2012, *MNRAS*, 427, 127.
- Cadelano, M., Pallanca, C., Ferraro, F. R., et al. 2017, *ApJ*, 844, 53
- Cadelano, M., Ransom, S. M., Freire, P. C. C., et al. 2018, *ApJ*, 855, 125
- Cadelano, M., Saracino, S., Dalessandro, E., et al. 2020, *ApJ*, 895, 54. doi:10.3847/1538-4357/ab88b3
- Calzetti, D., de Marchi, G., Paresce, F., et al. 1993, *ApJL*, 402, L1
- Cardelli, J. A., Clayton, G. C., & Mathis, J. S. 1989, *ApJ*, 345, 245.
- Casagrande, L. & Vandenberg, D. A. 2014, *MNRAS*, 444, 392.
- Clarkson, W. I., Sahu, K. C., Anderson, J., et al. 2011, *ApJ*, 735, 37. doi:10.1088/0004-637X/735/1/37
- Dalessandro, E., Ferraro, F. R., Massari, D., et al., 2013, *ApJ*, 778, 135
- Dalessandro, E., Pallanca, C., Ferraro, F. R., et al. 2014, *ApJL*, 784, L29

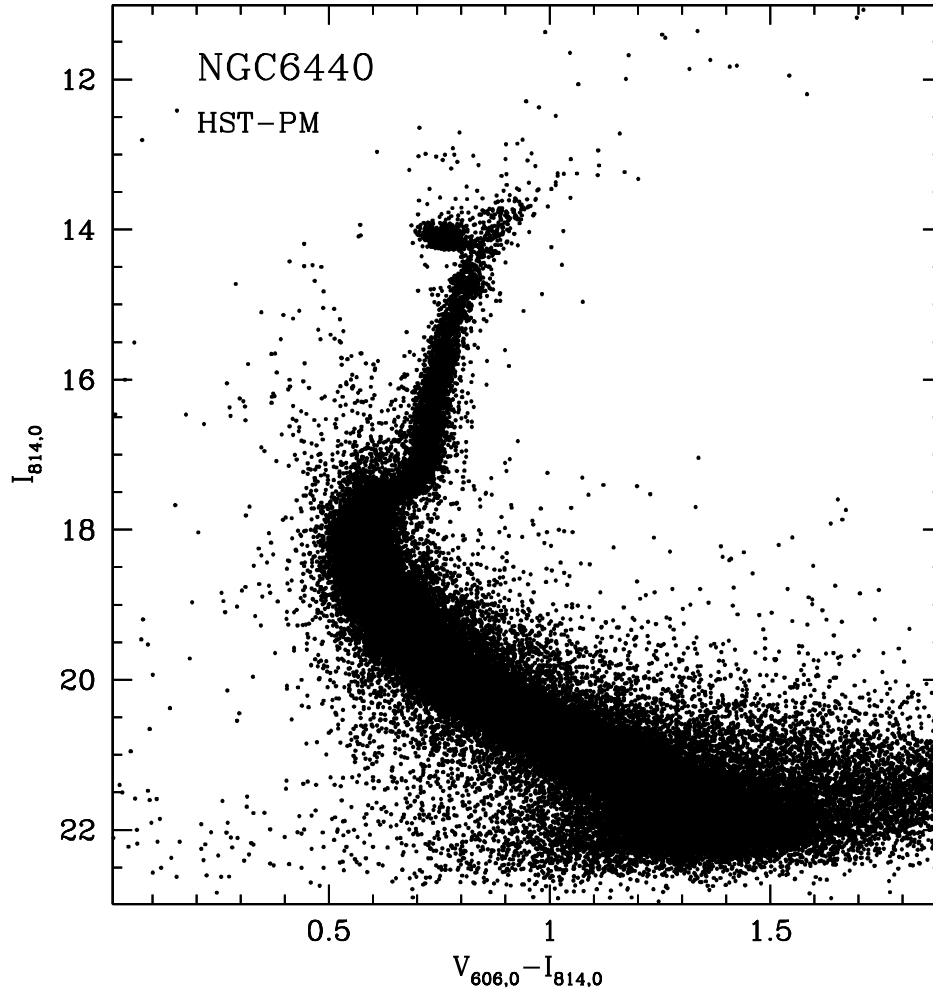


Figure 3. CMD of NGC 6440 from the *HST-PM* catalog. Only high-quality stars are plotted. Non-member stars (as determined from the proper motion analysis) have been removed. The magnitudes are corrected for the effect of reddening (Pallanca et al. 2019).

Djorgovski, S. 1993, Structure and Dynamics of Globular Clusters, 50, 373

Dotter, A., Chaboyer, B., Jevremović, D., et al. 2008, ApJS, 178, 89

Ferraro, F. R., Clementini, G., Fusi Pecci, et al. 1991, MNRAS, 252, 357

Ferraro, F. R., Fusi Pecci, F., Buonanno, R. 1992a, MNRAS, 256, 376

Ferraro, F. R., Clementini, G., Fusi Pecci, et al. 1992b, MNRAS, 256, 391

Ferraro, F. R., Paltrinieri, B., Fusi Pecci, et al. 1997a, A&A, 324, 915

Ferraro, F. R., Paltrinieri, B., Fusi Pecci, et al. 1997b, ApJ, 484, L145

Ferraro, F. R., Paltrinieri, B., Rood, R. T., et al. 1999a, ApJ, 522, 983

Ferraro, F. R., Messineo, M., Fusi Pecci, F., et al. 1999b, AJ, 118, 1738

Ferraro, F. R., Montegriffo, P., Origlia, L., et al. 2000, AJ, 119, 1282

Ferraro, F. R., Possenti, A., Sabbi, E., & D'Amico, N. 2003, ApJL, 596, L211

Ferraro, F. R., Beccari, G., Dalessandro, E., et al. 2009a, Nature, 462, 1028

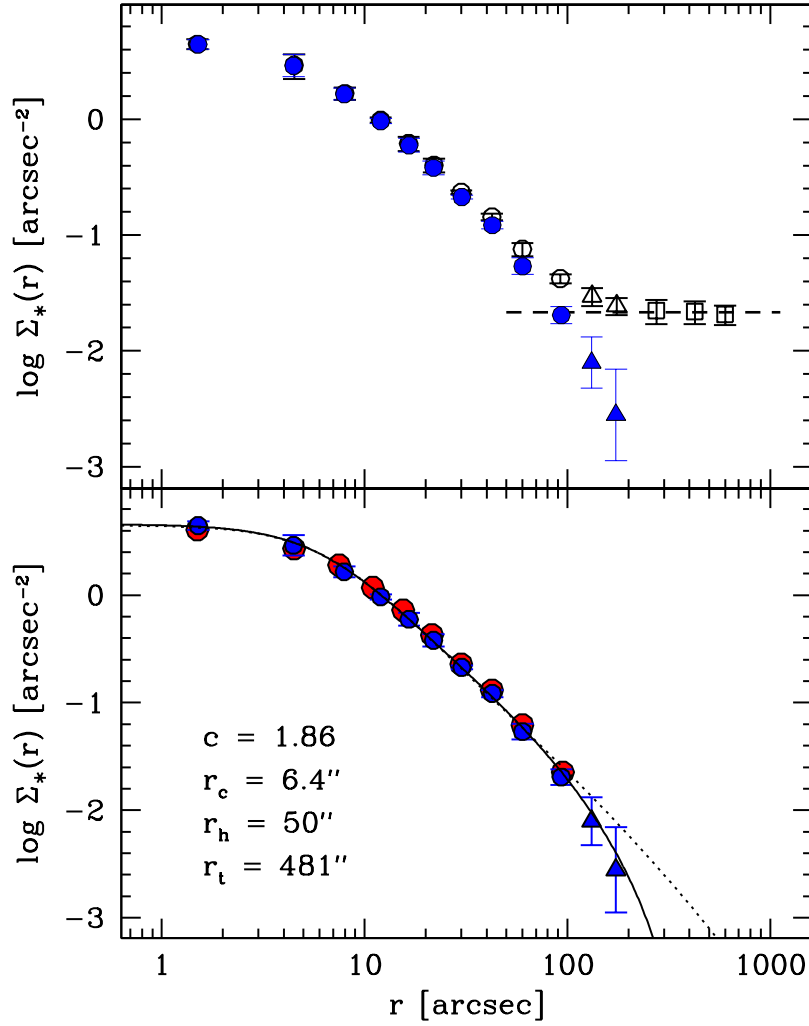


Figure 4. *Top:* Observed star density profile of NGC 6440 obtained from resolved star counts by combining three different catalogs: *HST-noPM* (empty circles), *FORS2* (empty triangles) and *Pan-STARRS* (empty squares). The filled blue symbols correspond to the cluster density profile obtained after subtraction of the Galaxy field contribution (dashed line). *Bottom:* Cluster density profile shown in the top panel (blue symbols) compared to that obtained from the *HST-PM* catalog (red circles). As can be seen the agreement is very good, thus guaranteeing the reliability of the applied background subtraction (see text). The black line shows the best-fit King model profile. The corresponding values of the concentration parameter (c) and a few characteristic scale-lengths (in arcseconds) are also labelled. The dotted line shows the best-fit Wilson model.

Ferraro, F. R., Dalessandro, E., Mucciarelli, A., et al. 2009b, *Nature*, 462, 483

Ferraro, F. R., Lanzoni, B., Dalessandro, E., et al. 2012, *Nature*, 492, 393

Ferraro, F. R., Lapenna, E., Mucciarelli, A., et al. 2016a, *ApJ*, 816, 70

Ferraro, F. R., Massari, D., Dalessandro, E., et al. 2016b, *ApJ*, 828, 75

Ferraro, F. R., Lanzoni, B., Raso, S., et al. 2018a, *ApJ*, 860, 36

Ferraro, F. R., Mucciarelli, A., Lanzoni, B., et al. 2018b, *ApJ*, 860, 50

Ferraro, F. R., Lanzoni, B., Dalessandro, E., et al. 2019, *Nature Astronomy*, 3, 1149

Ferraro, F. R., Pallanca, C., Lanzoni, B., et al. 2021, *Nature Astronomy*, 5, 311

Ferraro, F. R., Lanzoni, B., Dalessandro, E., 2020, *Rendiconti Lincei. Scienze Fisiche e Naturali*, 31, 19

Frogel, J. A., Stephens, A., Ramírez, S., et al. 2001, *AJ*, 122, 1896

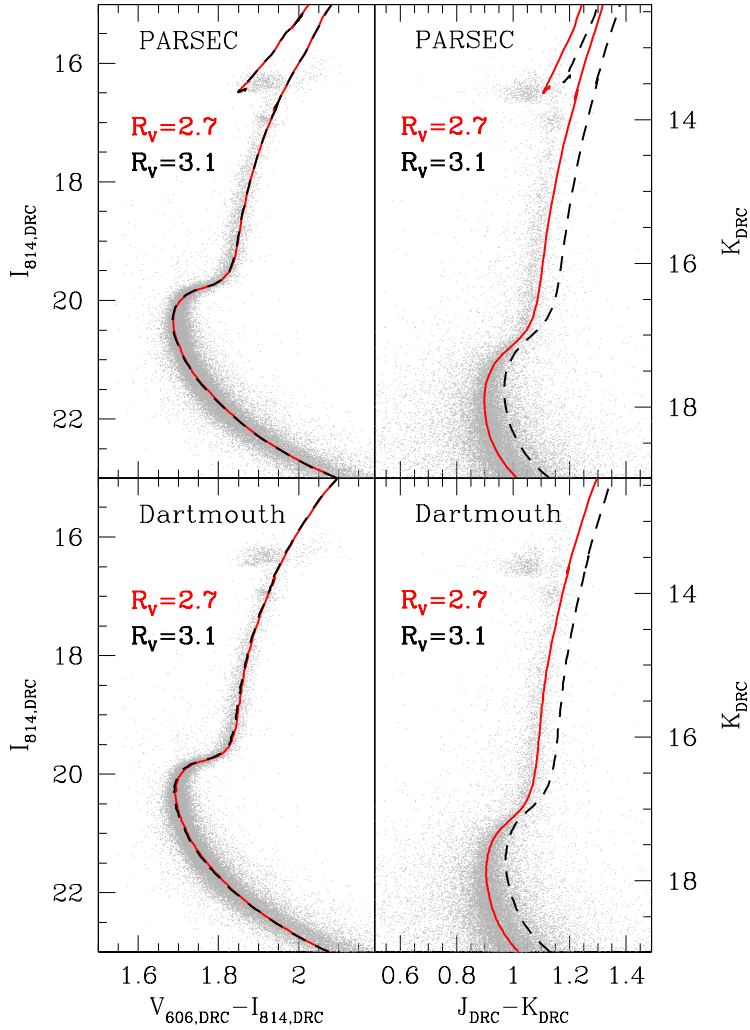


Figure 5. Comparison between the differential-reddening corrected CMD of NGC 6440 (grey dots) and theoretical isochrones computed for $R_V = 3.1$ (black dashed lines) and for $R_V = 2.7$ (red lines). The left and right panels show, respectively, the optical and the IR CMDs. The top panels refer to PARSEC isochrones, while the bottom panels show Dartmouth models. No solution able to properly fit the optical and the IR CMDs simultaneously is found for $R_V = 3.1$, while if $R_V = 2.7$ is assumed, both models well reproduce the observations for an age of 13 Gyr, a distance modulus of 14.60 and $E(B - V) = 1.26$ -1.28. The fact that the RGB looks steeper than the model in the IR CMDs may be due to nonlinearity effects of the GeMS/GSAOI photometry (see Saracino et al. 2016).

Fusi Pecci, F., Ferraro, F. R., Crocker, D.A., et al. 1990, A&A, 238, 95
 Gaia Collaboration, Brown, A. G. A., Vallenari, A., et al. 2016a, A&A, 595, A2
 Gaia Collaboration, Prusti, T., de Bruijne, J. H. J., et al. 2016b, A&A, 595, A1
 Giersz, M., Leigh, N., Hypki, A., et al. 2015, MNRAS, 454, 3150
 Gustafsson, B., Edvardsson, B., Eriksson, K., et al. 2008, A&A, 486, 951.

Harris, W. E. 1996, VizieR Online Data Catalog, 7195,
 Kerber, L. O., Libralato, M., Souza, S. O., et al. 2019, MNRAS, 484, 5530.
 King, I. R. 1966, AJ, 71, 64
 Kuchinski, L. E. & Frogel, J. A. 1995, AJ, 110, 2844.
 Lanzoni, B., Dalessandro, E., Ferraro, F. R., et al. 2007a, ApJ, 663, 267
 Lanzoni, B., Sanna, N., Ferraro, F. R., et al. 2007b, ApJ, 663, 1040

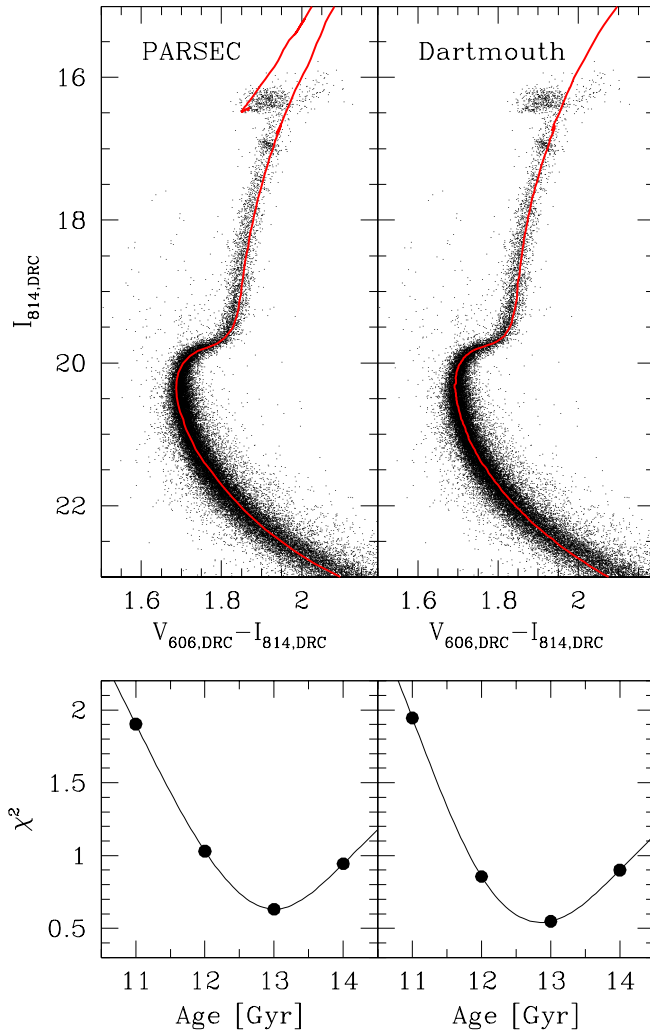


Figure 6. *Top panels:* differential-reddening corrected CMD of NGC 6440 with the best-fit isochrone from the PARSEC (left) and the Dartmouth (right) models superimposed as red lines (the same as in Figure 5). *Bottom panels:* value of the χ^2 parameter (see text) obtained from the fit of the SGB/MS-TO region through PARSEC (left) and Dartmouth (right) isochrones of 11, 12, 13, and 14 Gyr, as a function of the model age. The minimum of the χ^2 parameter is found for an age of 13 Gyr.

Lanzoni, B., Dalessandro, E., Ferraro, F. R., et al. 2007c, ApJL, 668, L139
 Lanzoni, B., Ferraro, F. R., Dalessandro, E., et al. 2010, ApJ, 717, 653
 Lanzoni, B., Ferraro, F. R., Alessandrini, E., et al. 2016, ApJL, 833, L29
 Lanzoni, B., Ferraro, F. R., Mucciarelli, A., et al. 2018a, ApJ, 865, 11
 Lanzoni, B., Ferraro, F. R., Mucciarelli, A., et al. 2018b, ApJ, 861, 16
 Lanzoni, B., Ferraro, F. R., Dalessandro, E., et al. 2019, ApJ, 887, 176

Lugger, P. M., Cohn, H. N., & Grindlay, J. E. 1995, ApJ, 439, 191
 Mackey, A. D., & Gilmore, G. F. 2003, MNRAS, 338, 85
 Massari, D., Mucciarelli, A., Ferraro, F. R. 2014, ApJ, 795, 22
 Mauro, F., Moni Bidin, C., Cohen, R., et al. 2012, ApJL, 761, L29.
 McCall, M. L. 2004, AJ, 128, 2144. doi:10.1086/424933
 McLaughlin, D. E., & van der Marel, R. P. 2005, ApJS, 161, 304
 Meylan, G., & Heggie, D. C. 1997, A&A Rv, 8, 1
 Minniti, D. 1995, A&A, 303, 468

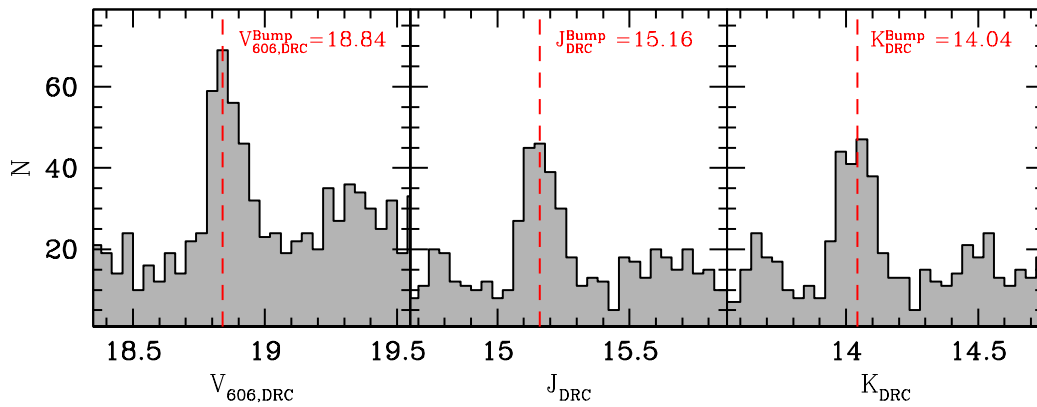


Figure 7. Differential luminosity function of RGB stars classified as cluster members and photometrically well measured. The detected peaks (marked by the dashed red lines) correspond to the RGB-bump magnitude in the three photometric bands (see labels).

- Miocchi, P., Lanzoni, B., Ferraro, F. R., et al. 2013, *ApJ*, 774, 151
- Montegriffo, P., Ferraro, F. R., Fusi Pecci, F., et al. 1995, *MNRAS*, 276, 739
- Muñoz, C., Villanova, S., Geisler, D., et al. 2017, *A&A*, 605, A12
- Nataf, D. M., Gould, A., Fouqué, P., et al. 2013a, *ApJ*, 769, 88
- Nataf, D. M., Gould, A. P., Pinsonneault, M. H., et al. 2013b, *ApJ*, 766, 77.
- Noyola, E., & Gebhardt, K. 2006, *AJ*, 132, 447
- Oliveira, R. A. P., Souza, S. O., Kerber, L. O., et al. 2020, *ApJ*, 891, 37.
- Origlia, L., Ferraro, F. R., Fusi Pecci, F., et al. 1997, *A&A*, 321, 859
- Origlia, L., Valenti, E., & Rich, R. M. 2008a, *MNRAS*, 388, 1419
- Origlia, L., Lena, S., Diolaiti, E., et al. 2008b, *ApJ*, 687, L79
- Origlia, L., Rich, R. M., Ferraro, F. R., et al. 2011, *ApJ*, 726, L20
- Ortolani, S., Barbuy, B., & Bica, E. 1994, *A&AS*, 108, 653
- Pallanca, C., Dalessandro, E., Ferraro, F. R., et al. 2010, *ApJ*, 725, 1165
- Pallanca, C., Dalessandro, E., Ferraro, F. R., Lanzoni, B., & Beccari, G. 2013, *ApJ*, 773, 122

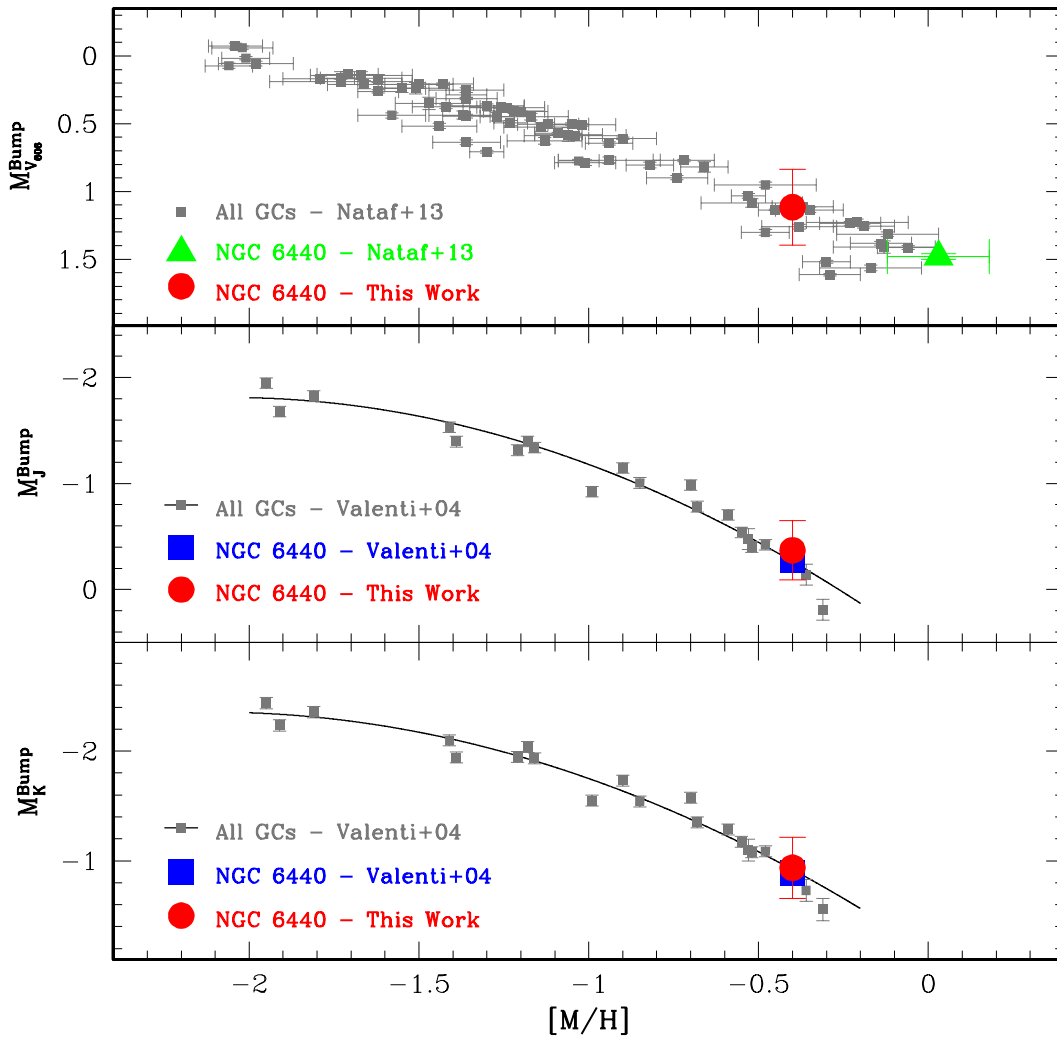


Figure 8. Absolute magnitude of the RGB-bump in the V_{606} , J and K bands (from top to bottom) as a function of the GC global metallicity $[M/H]$. The gray symbols are from the literature (see labels). The blue squares and the green triangle mark the location of NGC 6440 according to literature (Nataf et al. 2013b; Valenti et al. 2004b) while the red circle mark the values determined in this work.

Pallanca, C., Ransom, S. M., Ferraro, F. R., et al. 2014, ApJ, 795, 29

Pallanca, C., Beccari, G., Ferraro, F. R., et al. 2017, ApJ, 845, 4

Pallanca, C., Ferraro, F. R., Lanzoni, B., et al. 2019, ApJ, 882, 159

Picard, A. & Johnston, H. M. 1995, A&AS, 112, 89

Pooley, D., Lewin, W. H. G., Anderson, S. F., et al. 2003, ApJL, 591, L131

Popowski, P. 2000, ApJL, 528, L9

Portegies Zwart, S. F., Baumgardt, H., Hut, P., Makino, J., & McMillan, S. L. W. 2004, Nature, 428, 724

Ransom, S. M., Hessels, J. W. T., Stairs, I. H., et al. 2005, Science, 307, 892

Raso, S., Ferraro, F. R., Dalessandro, E., et al. 2017, ApJ, 839, 64

Riello, M., Cassisi, S., Piotto, G., et al. 2003, A&A, 410, 553.

Salinas, R., Jílková, L., Carraro, G., et al. 2012, MNRAS, 421, 960

Santos, J. F. C., Maia, F. F. S., Dias, B., et al. 2020, MNRAS, 498, 205.

Saracino, S., Dalessandro, E., Ferraro, F. R., et al. 2015, ApJ, 806, 152

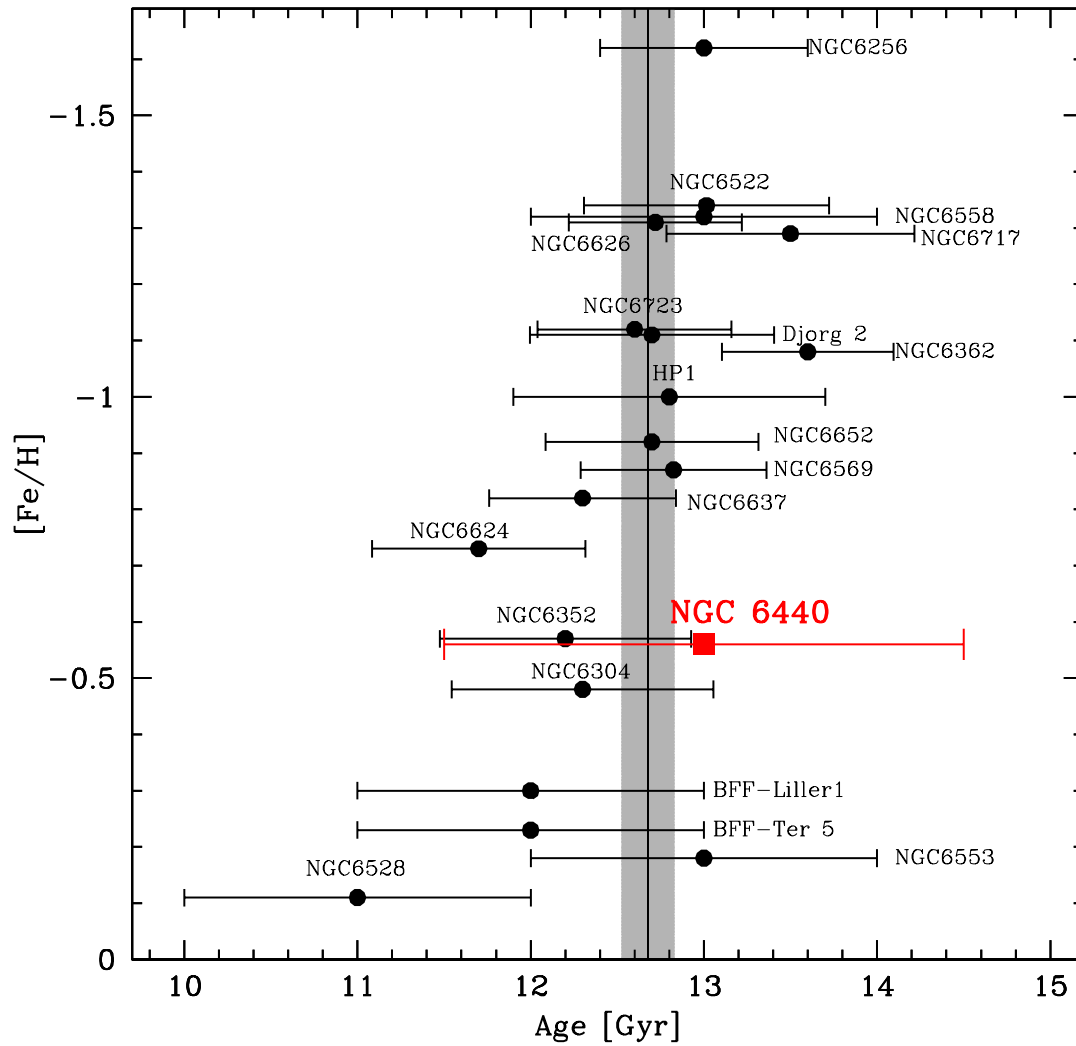


Figure 9. Age-metallicity distribution for the bulge GCs with age estimate available. NGC 6440 is marked as a large red square. Data for the other clusters are mainly from Saracino et al. (2019, see their Figure 16) and Oliveira et al. (2020, see their Figure 12) with the addition of the recent age determination of NGC 6256 (Cadelano et al. 2020). We also plotted the age-metallicity of the oldest stellar population in the two Bulge Fossil Fragments (BFF; namely Terzan5 and Liller1) so far discovered into the bulge (Ferraro et al. 2009b, 2016b, 2021). The grey vertical strip marks the weighted average and 1σ uncertainty (12.7 ± 0.2 Gyr) of the entire sample.

Saracino, S., Dalessandro, E., Ferraro, F. R., et al. 2016, ApJ, 832, 48.

Saracino, S., Dalessandro, E., Ferraro, F. R., et al. 2019, ApJ, 874, 86.

Stetson, P. B. 1987, PASP, 99, 191

Stetson, P. B. 1994, PASP, 106, 250

Udalski, A. 2003, ApJ, 590, 284.

Valenti, E., Ferraro, F. R., & Origlia, L. 2004a, MNRAS, 351, 1204

Valenti, E., Ferraro, F. R., & Origlia, L. 2004b, MNRAS, 354, 815.

Valenti, E., Zoccali, M., Renzini, A., et al. 2013, A&A, 559, A98.

Wilson, C. P. 1975, AJ, 80, 175

Zoccali, M., Cassisi, S., Piotto, G., et al. 1999, ApJL, 518, L49.

Zoccali, M., Renzini, A., Ortolani, S., et al. 2003, A&A, 399, 931.

Table 2. Identity card of NGC 6440: new determinations of its basic parameters.

Parameter	Estimated value
Center of gravity	$\alpha_{J2000} = 17^{\text{h}}48^{\text{m}}52.84^{\text{s}}$ $\delta_{J2000} = -20^{\circ}21'37.5''$
Reddening law	$R_V = 2.7$
Color excess	$E(B - V) = 1.26 - 1.28$
Distance modulus	$\mu_0 = 14.6 \pm 0.1$
Distance	$d = 8.3 \pm 0.4$ kpc
Age	$t = 13 \pm 1.5$ Gyr
RGB bump	$M_{V606}^{\text{Bump}} = 1.12 \pm 0.12$ $M_J^{\text{Bump}} = -0.37 \pm 0.12$ $M_K^{\text{Bump}} = -0.94 \pm 0.12$
Dimensionless central potential	$W_0 = 8.10_{-0.20}^{0.20}$
Concentration parameter	$c = 1.86_{-0.06}^{0.06}$
Core radius	$r_c = 6.4_{-0.3}^{0.3}$ arcsec = $0.26_{-0.01}^{0.01}$ pc
Half-mass radius	$r_h = 50.2_{-4.5}^{5.2}$ arcsec = $2.02_{-0.18}^{0.21}$ pc
Effective radius	$r_e = 36.8_{-3.2}^{3.7}$ arcsec = $1.48_{-0.13}^{0.15}$ pc
Truncation radius	$r_t = 481.4_{-42.3}^{43.9}$ arcsec = $19.4_{-1.7}^{1.8}$ pc
Central relaxation time	$\log(t_{rc}/\text{yr}) = 7.4$
Half-mass relaxation time	$\log(t_{rh}/\text{yr}) = 9.0$